RL-TR-96-206
Final Technical Report
December 1996

POLARIZATION AND PHOTOMETRIC METHODS IN MACHINE VISION

The John Hopkins University

DTIC QUALITY INSPECTED 3

19970218 035

APPROVED FOR PUBLIC RELEASE; DISTRIBUTION UNLIMITED.

The views and conclusions contained in this document are those of the authors and should not be interpreted as necessarily representing the official policies, either expressed or implied, of the Advanced Research Projects Agency or the U.S. Government.

**Rome Laboratory
Air Force Materiel Command
Rome, New York**

This report has been reviewed by the Rome Laboratory Public Affairs Office (PA) and is releasable to the National Technical Information Service (NTIS). At NTIS it will be releasable to the general public, including foreign nations.

RL-TR-96-206 has been reviewed and is approved for publication.
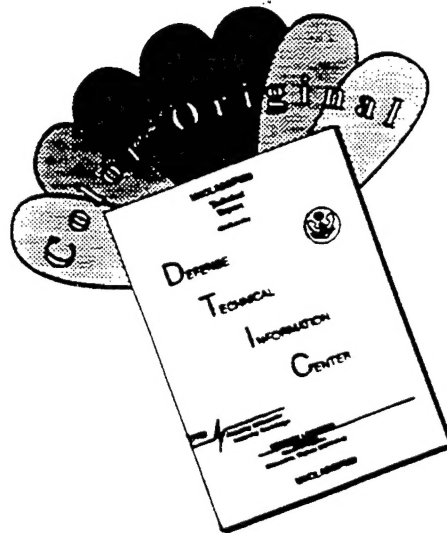
APPROVED: *Peter J. Costianes*

PETER J. COSTIANES
Project Engineer

FOR THE COMMANDER: *Joseph Camera*

JOSEPH CAMERA
Technical Director
Intelligence & Reconnaissance Directorate

DISCLAIMER NOTICE

THIS DOCUMENT IS BEST QUALITY AVAILABLE. THE COPY FURNISHED TO DTIC CONTAINED A SIGNIFICANT NUMBER OF COLOR PAGES WHICH DO NOT REPRODUCE LEGIBLY ON BLACK AND WHITE MICROFICHE.

POLARIZATION AND PHOTOMETRIC METHODS IN
MACHINE VISION

Contractor: The John Hopkins University
Contract Number: F30602-92-C-0191
Effective Date of Contract: 29 July 1992
Contract Expiration Date: 28 July 1996
Program Code Number: 3E20
Short Title of Work: Polarization and Photometric Methods
                       in Machine Vision

Period of Work Covered: Jul 92 - Jul 96

Principal Investigator: Dr. Lawrence B. Wolff
              Phone: (410) 516-8710

RL Project Engineer: Peter J. Costianes
              Phone: (315) 330-4863

REPORT DOCUMENTATION PAGE

Form Approved
OMB No. 0704-0188

1. AGENCY USE ONLY (Leave Blank)	2. REPORT DATE December 1996	3. REPORT TYPE AND DATES COVERED Final Jul 92 - Jul 96

4. TITLE AND SUBTITLE	5. FUNDING NUMBERS
Polarization and Photometric Methods in Machine Vision	C - F30602-92-C-0191 PE - 62301E
6. AUTHOR(S) Dr. Lawrence B. Wolff	PR - H735 TA - 00 WU - 01

7. PERFORMING ORGANIZATION NAME(S) AND ADDRESS(ES)	8. PERFORMING ORGANIZATION REPORT NUMBER
The John Hopkins University Computer Vision Laboratory, Dept of Computer Science Baltimore MD 21218	N/A

9. SPONSORING/MONITORING AGENCY NAME(S) AND ADDRESS(ES)	10. SPONSORING/MONITORING AGENCY REPORT NUMBER
DARPA/ISO Rome Laboratory/IRRE 3701 N. Fairfax Drive 32 Hangar Road Arlington VA 22203-1714 Rome NY 13441-4114	RL-TR-96- 206

11. SUPPLEMENTARY NOTES

RL Project Engineer: Mr. Peter J. Costianes/IRRE/ (315) 330-4863

12a. DISTRIBUTION/AVAILABILITY STATEMENT	12b. DISTRIBUTION CODE
Approved for public release; distribution unlimited.	

13. ABSTRACT (Maximum 200 words)

Described in this report are designs for polarization camera sensors that have been built to automatically sense partially linearly polarized light, and computationally process this sensed polarization information at pixel resolution to produce a visualization of reflected polarization from a scene, and/or, a visualization of physical information in a scene directly related to sensed polarization. The research performed on polarization-based methods in computer and machine vision provides a new powerful medium for object feature extraction with tremendous versatility and a broad range of applications. The fundamental principles behind these polarization methods developed under this effort are easy to implement with the simple addition of a linear polarizing filter to a standard off-the-shelf camera sensor. We present a fully automatic polarization camera using liquid crystal technology. Not only are polarization-based feature extraction methods passive, but they require little prior knowledge about the world environment. This makes polarization-based methods applicable beyond just the controlled environments of machine vision.

14. SUBJECT TERMS		15. NUMBER OF PAGES 50
Optical polarization, machine vision, vision extraction		16. PRICE CODE

17. SECURITY CLASSIFICATION OF REPORT UNCLASSIFIED	18. SECURITY CLASSIFICATION OF THIS PAGE UNCLASSIFIED	19. SECURITY CLASSIFICATION OF ABSTRACT UNCLASSIFIED	20. LIMITATION OF ABSTRACT SAR

1 Polarization Vision

1.1 Introduction

One of the fundamental properties of light is polarization. Polarization of light radiation has been used as an important measurement tool for the study of a number of phenomena in astronomy, optics, and, crystallography. Only recently has the measurement of polarization been considered for use in imagery [1], [2], [3]. In [4] a number of research results were presented demonstrating that the sensing of reflected polarization can directly enhance the capabilities and/or simplify certain important Image Understanding tasks beyond what intensity and color can accomplish alone. This was shown to be true for tasks such as dielectric/metal discrimination in images, detection of specularities (i.e., glossy highlights), quantitative separation of specular and diffuse reflections, and, direct identification of occluding contours (i.e., edge boundaries between object and background). Furthermore while these were a diverse set of applications, all these methods arose from the same physical principles governing the polarization of reflected light from both dielectric and metal surfaces. The key new perspective that came out of this work with respect to the role of polarization sensing in Image Understanding was that polarization being orthogonal to wavelength (i.e., color) and a more general physical characteristic of light than intensity can carry additional information and therefore provide a richer description of an imaged scene. Therefore, the use of polarization for Image Understanding is an augmentation of sensed light parameters from a scene that can have significantly more capabilities than intensity and color alone. "Polarization Vision" is an area that could potentially play a mainstream role in Computer Vision.

The practical significance of the enhanced capabilities of Polarization Vision was still hindered by the fact that commercially available video imaging cameras are geared to sense only intensity and color. The sensing of polarization requires optical components that are not available in existing video cameras for Computer Vision. Past results have almost always used a monochrome or color CCD camera with a mechanically rotating linear polarizing filter placed in front of the camera lens. Multiple images have been obtained with respect to different orientations of the polarizing filter- at least three polarization component images are required for a complete measurement of partial linear polarization. While producing some good results, this design for a polarization imaging device is cumbersome both from a practical and a conceptual standpoint. The mechanical rotation of an optical filter in front of an imaging camera causes slight geometric shifting of the projection of the world scene onto the focal plane, and where there are significant local intensity variations in a scene (e.g., edges) the shifting of these intensity variations across pixels between polarization component images causes significant error in polarization measurement. At least as important, real-time applications outside the laboratory are difficult using this type of design. The mechanical rotation of a polarizing filter gives Polarization Vision the appearance of being a multiple

view modality, when in fact conceptually the measurement of polarization need not involve multiple views any more than the measurement of color.

In [4] a high-level description was given for a *Polarization Camera* that would fully automatically sense polarization components of light in a passive fashion without mechanical manipulation of external optics. This would make the enhanced capabilities of Polarization Vision accessible to a larger diversity of Image Understanding applications. The first working prototype of a Polarization Camera was presented in [5], [6], [7] utilizing liquid crystal technology. This was presented in conjunction with a visually intuitive representation scheme for partial linear polarization images. In the 1970s biologists Bernard and Wehner [8] conjectured that polarization vision in certain animals could be analogous to color vision in humans. In [5], [6] a representation scheme was developed from this conjecture for measured partial linear polarization at pixels in digital images in terms of the saturation of a color hue. To Computer Vision researchers this was a significant step because instead of measured polarization parameters being just a set of abstract numbers, humans can actually "see" Polarization Vision measured by a polarization camera as being a natural visual domain unto itself. An overview of a number of prototype designs for Polarization Cameras are presented in [9].

This subsection overviews significant new developments in Polarization Vision resulting from the application of Polarization Camera Technology to a number of real practical problems for Image Understanding outdoors and underwater. The system advancements that have made these applications possible are the low-cost modular designs of compact optical and electronic components that can be used with almost any kind of imaging device. Utilizing our visualization scheme for polarization images, Polarization Cameras are giving humans for the first time a comprehensive sensory view of a whole new visual domain which is speculated to be as broad an area in both theoretical and practical significance as color vision is an extension to intensity vision.

1.2   Brief Polarization Background

The left of Figure 1 shows the electric field distribution of partially linear polarized light viewed head-on as the superposition of an *unpolarized* component consisting of an isotropic electric field distribution, with a *linear polarized* component consisting of an electric field oriented along a single axis. Humans only visually perceive the energy flux of this distribution as "intensity". What is not visually perceived are the relative magnitudes of unpolarized and linear polarized components that constitute the light, nor the orientation of the axis of linear polarization if there is such a non-zero component. The relative proportion of linear polarization we will term the *partial polarization* varying between 0 (completely unpolarized light) and 1 (completely linearly polarized light). Partial polarization is also known as the *degree of polarization* [10]. The orientation of linear polarization we will term the *phase* or

Visualizing Polarization

Length of Hue vector = partial polarization

Blue   Cyan

2θ

Magenta   Green

Intensity = Image Intensity

Red   Yellow

Orientation Reference Axis

θ
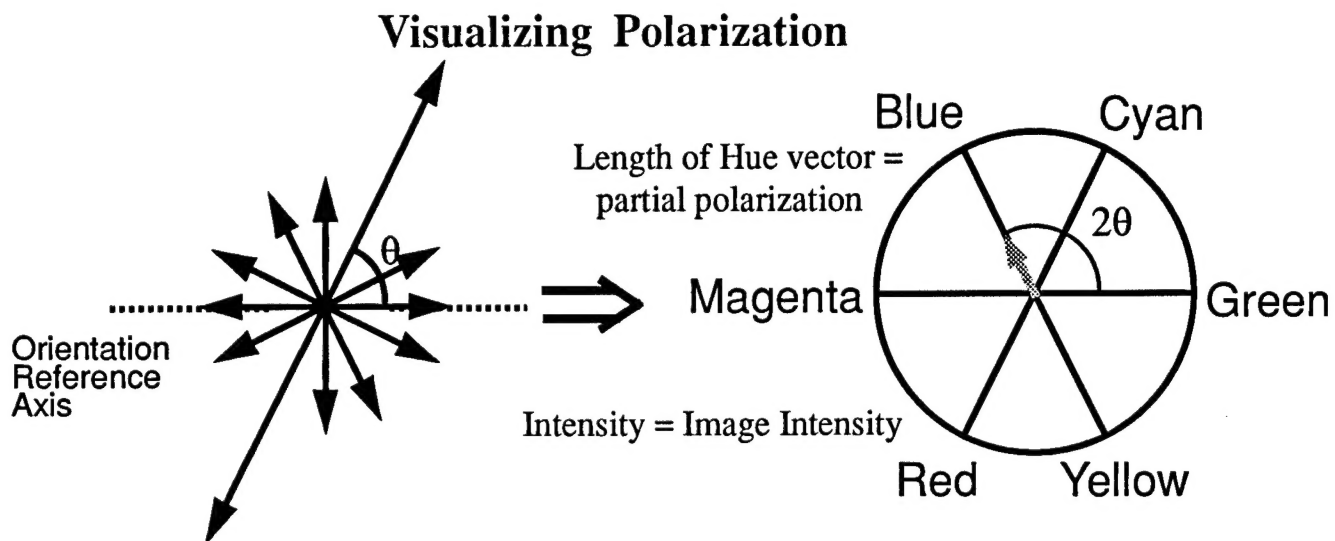
Figure 1: Hue-saturation-intensity representation scheme for partial linear polarization.

Twisted Nematic Liquid Crystal

Plane of Linear Polarization Twisted Counterclockwise after Passing Through Crystal

Plane of Component of Linear Polarization

Twisting
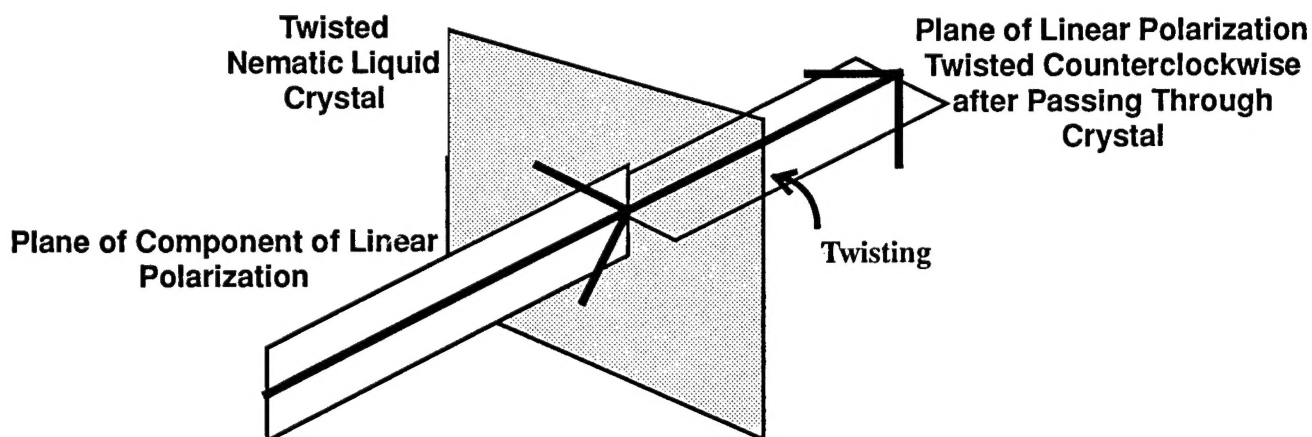
Figure 2: Rotation of the linear polarized component of polarization by a TN liquid crystal.

Modulated AC Signal

Electronic Driver Box

Output Sync to Digitizing Board, or Audio Track

Fixed Linear Polarizer

Optical Head

NTSC Video Imaging Device

Video Out

Twisted Nematic Liquid Crystals

Figure 3: Schematic of an optical head and electronic box interfaced with an NTSC Imaging Device giving it automatic polarization sensing capability.

3

simply the *orientation* of polarization. Note that the phase varies within the range $0 - 180^{\circ}$. Together the param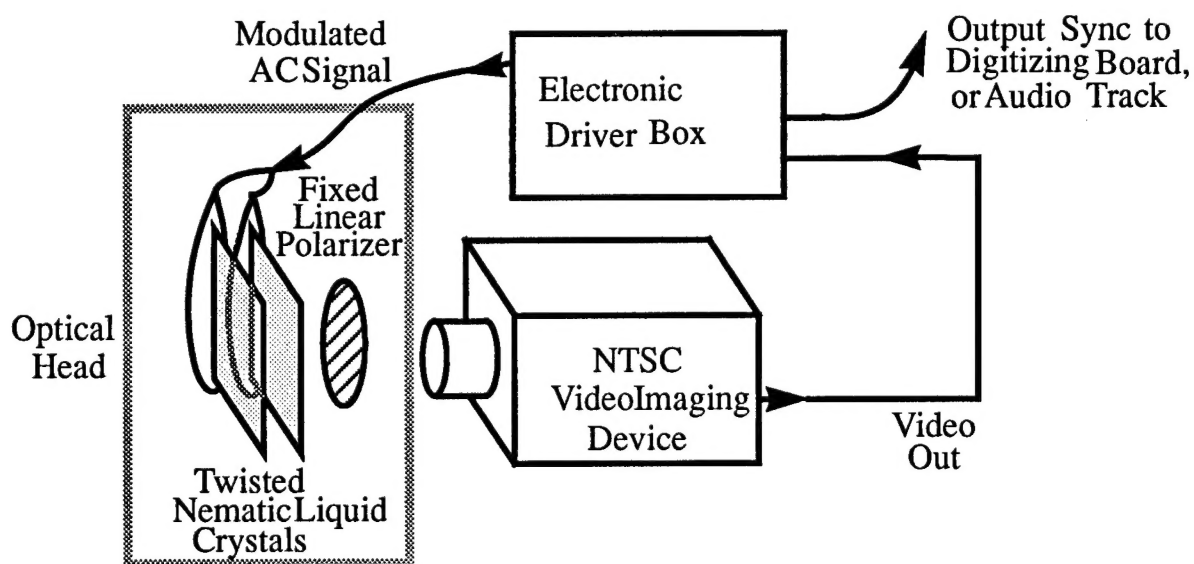eters (i) intensity, (ii) partial polarization, and, (iii) phase, completely determine the state of partial linear polarization. Parameters (ii) and (iii) are the sensory augmentation beyond conventional intensity and color vision. A precise definition of polarization is presented in [10].

In general polarization of light can have a fourth parameter which describes an elliptically polarized light component of which linear polarization is a particular case. There are some benefits to measuring this fourth parameter of polarization, as explained in [1] for determination of surface orientation, and in [4] for dielectric/metal discrimination. However, studies by Waterman [11] and other researchers have shown that almost all naturally occurring light outdoors and underwater, scattered and reflected, as well as light in most indoor environments is partially linear polarized. While we have extended the designs for Polarization Cameras to measure all four polarization parameters, we have found little reason in our applications so far to use such designs. Polarization Cameras that measure partial linear polarization have proven to be quite sufficient.

A state of partial linear polarization can be measured using a linear polarizing filter which resolves the electric field distribution of light along a given orientation. At a pixel in an image the transmitted radiance of partially linear polarized light through a linear polarizing filter varies sinusoidally with period 180° as a function of polarizer orientation. The maximum, I_{max}, of the sinusoid occurs when polarizer orientation is aligned parallel to the orientation of the linear polarized component, and the minimum, I_{min}, occurs when polarizer orientation is aligned perpendicular to the linear polarized component. With no linear polarized component the sinusoid is simply a horizontal line with one-half the intensity magnitude of the unpolarized light. With no unpolarized component the minimum value of the sinusoid is 0. Since a sinusoid can be uniquely determined by three points, three transmitted radiance measurements can be taken between 0° and 180° to determine partial linear polarization. We have standardly taken measurements at 0°, 45°, and 90°. Representing these measurements respectively by I_0, I_{45}, and, I_{90}, the three parameters of partial linear polarization can be derived according to:

$$\text{phase } \theta = (1/2)\tan^{-1}(\frac{I_0 + I_{90} - 2I_{45}}{I_{90} - I_0}) + 90, \tag{1}$$

$$\text{if } (I_{90} < I_0) \ [\ \text{if } (I_{45} < I_0) \ \theta = \theta + 90 \text{ else } \theta = \theta - 90]$$

$$\text{intensity} = I_0 + I_{90}, \tag{2}$$

$$\text{partial polarization} = \frac{I_{90} - I_0}{(I_{90} + I_0)\cos 2\theta}. \tag{3}$$

In previous publications the convention has been used that the phase angle θ represent the angle at which the minimum I_{min} is observed for the sinusoid of transmitted radiance,

4

relative to the reference 0°. Geometrically this makes the phase angle perpendicular to the orientation of the linear polarized component. In this paper we add a 90° term in expression (1) using the more intuitive convention that makes the phase angle parallel with the linear polarized component.

Figure 1 shows a mapping of partial linear polarization into a hue-saturation-intensity visualization scheme proposed in [5], [6]. Phase and partial polarization which are not observed by human vision are represented respectively in terms of hue and saturation. Since phase of polarization is in the range $0 - 180^o$, phase angle is multiplied by two to map into the entire range of hue representation. An image for which the measurement of polarization at each pixel is represented according to the scheme depicted in Figure 1 will be termed a *partial linear polarization image*, or simply a *polarization image*. Chromaticity at a pixel in a polarization image means that there is some presence of linear polarization as saturation corresponds directly to partial polarization. Unpolarized light at a pixel in a polarization image is therefore achromatic. Intensity is of course simply intensity itself.

We analyzed monochrome polarization images, meaning that the measured polarization state at each pixel is taken over a single range of wavelengths. Of course multiple polarization images can be respectively taken over different spectral wavelength ranges adding even more sensed information. It can be difficult to visualize a vision system that is simultaneously sensitive to intensity, color, and, polarization. Photometrically human vision is three dimensional at each spatial point- two dimensions for color (i.e., hue and saturation), and one dimension for brightness. Adding partial linear polarization sensing would make for a vision system which is five dimensional. It turns out that some animals, such as the Mantis Shrimp [12], may possess such higher dimensional photometric vision systems. Images simultaneously visualizing intensity, color and polarization can, for instance, incorporate texture or dithering patterns at pixels that represent states of polarization.

There are two physical principles of reflected polarization which are basic to Polarization Vision [4], [13]. The *plane of incidence* at an object point viewed by a camera sensor is determined by the surface normal at the point and the viewing direction.

- For unpolarized incident light, specular reflection (i.e., glossy reflection) has non-zero partial polarization, except for normal and grazing incidence, with linear polarized component oriented *perpendicular* to the plane of incidence.

- Diffuse reflection from dielectric surfaces for most viewing angles is essentially unpolarized, becoming significantly partially polarized at greater than 60° with respect to the angle between the viewing direction and the surface normal. The orientation of the linear polarized component is *parallel* to the plane of incidence for diffuse reflection. For smooth dielectric surfaces this is true for any incident polarization state.

1.3 Portable Polarization Camera Sensors From Modular Components

In [5], [6] a prototype Liquid Crystal Polarization Camera was developed for full automatic accurate capture of polarization imagery in the laboratory under computer control. The electro-optical switching of Twisted Nematic (TN) liquid crystals in front of a fixed linear polarizer obviates the need for mechanically rotating the linear polarizer for obtaining polarization component images with an intensity video camera. When an AC signal is passed through each of the liquid crystals, the polarization state of light passing through the crystals is unaltered – with no voltage the linear polarized component of incident light is rotated by a fixed amount n^o, the value n determined when the TN liquid crystal is fabricated. See Figure 2. The two TN liquid crystals used are respectively 45° and 90° twist. A timing circuit places the switching of the liquid crystals in synchronization with camera video rate, and in series the two liquid crystals can produce 0°, 45°, 90° and 135° twist states at which times an image is digitized – only the first three states are used to completely measure partial linear polarization. What used to be done by mechanical rotation of a linear polarizing filter is now done electro-optically using liquid crystals and a fixed linear polarizing filter, which does not produce optical distortion. The switching and grabbing of polarization component images is placed under full electrical/computer control. The switching of the liquid crystals in synchronization with video framerate insures that polarization components are imaged when the liquid crystals are in a fully "relaxed" state as well as knowing which liquid crystal state corresponds to each imaged polarization component. The original TN liquid crystals in [5], [6], required 1/10 second (three 1/30 second video frametimes) to switch states and then a fourth video frametime to grab the image. With twelve video frametimes to grab a complete set of three polarization component images, polarization images were sensed at 2.5 Hz.

Current TN liquid crystals switch in less than a video frametime– now only one frametime is used to switch states and one frametime to grab the polarization component image. At two video frametimes to sense each polarization component image, 15 component images can be sensed in a second. With six video frametimes to grab a complete set of three polarization component images, polarization images can now be sensed at 5 Hz (one polarization image every 0.2 seconds). If only fields are used at half image resolution (the interlacing of a field consisting of even numbered raster lines, and a field consisting of odd numbered raster lines, makes up an entire frame) the speed doubles to 10Hz for the sensing of partial linear polarization images. The design for the original prototype Liquid Crystal Polarization Camera has been adapted for portable use outdoors and underwater by designing modular and compact components that are compatible with any standard NTSC video imaging device. The two main modular components that have been designed are:

- (I) the coupling of the liquid crystals and fixed linear polarizer to form a small optical

6

head that can be easily mounted on any camera lens,

- (II) the design of a compact electronic box that drives the liquid crystals in synchronization with the video rate of the NTSC imaging device, as well as corresponding polarization component images with the state of the liquid crystals when they were imaged.

TN liquid crystals are low-power only requiring a 9-volt battery to operate the electronics that drive them. Furthermore these liquid crystals are relatively low cost. Figure 3 shows a high level schematic of how the optical head and electronic box are interfaced with an NTSC video imaging device.

A number of processing options utilizing equations (1), (2), and, (3), have been used depending upon suitability for particular applications. When using a digitizing board along the backplane of a host computer two possibilities are useful; (i) a single sequence of three polarization component images are sensed, digitized and then processed to produce a single polarization image; (ii) a sequence of polarization images can be computed on the fly using real-time processor hardware (e.g, Datacube MV-200 can incorporate equations (1), (2), and, (3) into look-up tables) with either a polarization image updated 5 times a second after the completion of each sequence of 0°, 45°, 90° polarization component images, or, a piplineing scheme in which a polarization image is updated 15 times a second processing the most recently sensed three polarization component images each time. The 15Hz polarization image capability of this pipelining scheme is deceptive though– each element in a scene must remain relatively static for 1/5 second (6 video frametimes) for a complete sequence of three polarization images to be sensed, otherwise polarization measurement will be in error. Partial linear polarization sensing is still at 5Hz with respect to a scene in which objects are in movement. Using a video camcorder polarization component images are stored on video tape which can then be later digitized and processed back in the laboratory using schemes (i), or, (ii) discussed above. Since camcorders are very portable, and a large amount of image data can be stored on a single video tape, they provide a very convenient polarization camera for field use. The only drawbacks to using a video camcorder is slightly less polarization image quality due to the double process of sensing off of video tape and then digitizing, and, Hi-8 high resolution video format is limited to 400 scanlines. Nonetheless we have obtained excellent results using camcorders.

Figure 4 shows a portable version of a Liquid Crystal Polarization Camera using a small HI-8 Video Camcorder. The two modular components described above can be clearly seen here with the liquid crystal/polarizer optical head mounted on the Camcorder, and the compact white electronic box containing the timing circuitry that synchronizes and drives the liquid crystals, to the right.

Figure 5 shows a similar liquid crystal/linear polarizer optical head mounted on a CCD video camera that has been encased in a waterproof housing. This was developed under the
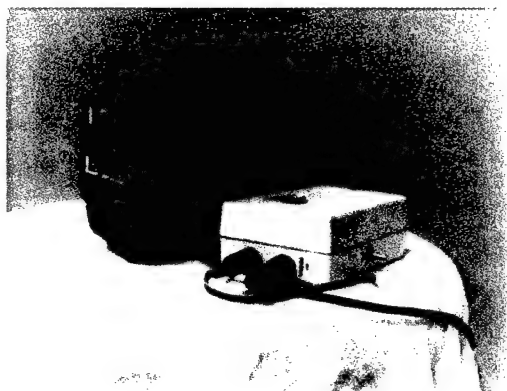
Figure 4: Liquid Crystal Polarization Camera using a Video Camcorder.
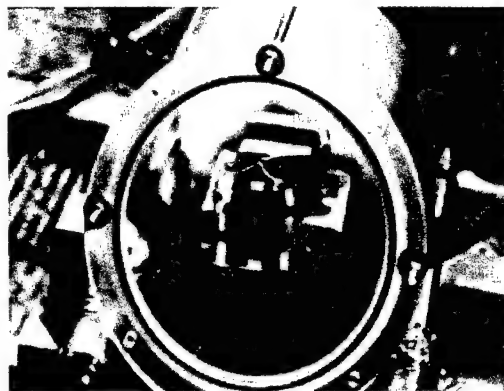
Figure 5: Liquid Crystal Polarization Camera for underwater use. sponsored by U.S. Coast Guard.
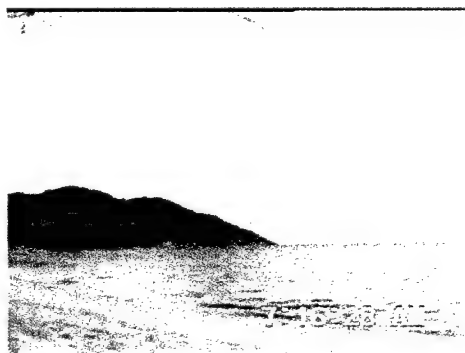
Figure 6: Intensity image of beach scene at sunrise.

Figure 7: Polarization image of beach scene at sunrise.

Figure 8: Intensity image of beach scene at sunset.

Figure 9: Polarization image of beach scene at sunset.

Figure 10: Intensity image of river running through wooded hills under cloudy sky.

Figure 11: Polarization-based segmentation of river (Magenta).

7A

Figure 12: Intensity image of grass and dirt terrain with protruding rock.

Figure 13: Polarization-based segmentation of dirt (Red) and protruding rock (Green).

Figure 14: Intensity image of camouflaged HMMWV partially occluded by a bush.

Figure 15: Polarization-based segmentation of highly polarization reflecting camouflage resulting in target detection (Magenta).

Figure 16: Intensity image of a HMMWV.
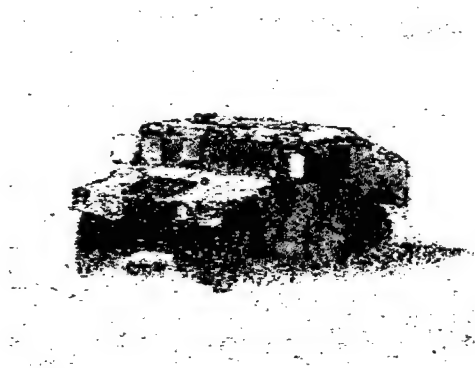
Figure 17: Polarization image of HMMWV.. Polarization features provide additional target recognition capability.
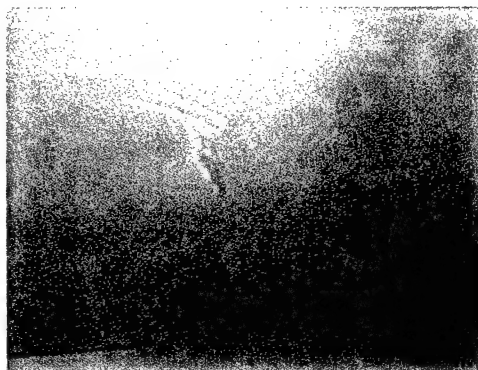
Figure 18: Intensity image of scraped painted steel panel.
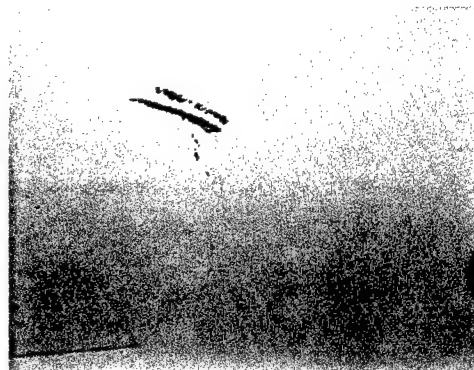
Figure 19: Polarization based segmentation of metal (Green) and superficial (Magenta) scrapes.
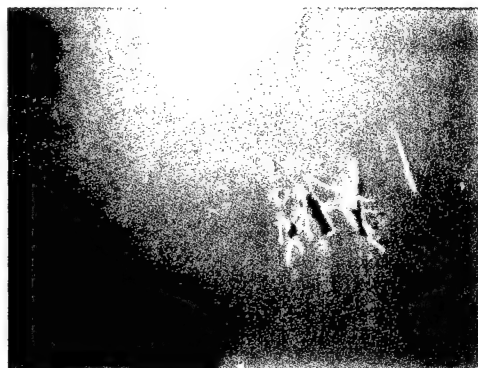
Figure 20: Intesnity image of rusted and scrape steel panel.

Figure 21:Polarization based segmentation of rust (Yellow) and superficial scrapes (Magenta).

Figure 22: Color image of fish underwater.
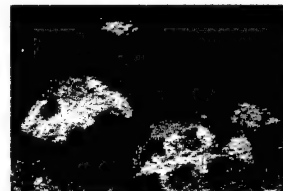
Figure 23: Polarization image of fish underwater

Figure 24: Polarization image of Mantis Shrimp underwater.

sponsorship of the U.S. Coast Guard, and is being used at the Naval Surface Warfare Center, Annapolis, Maryland, in underwater test tanks and river basins to study automated ship hull damage assessment. In this setup a sequence of three polarization component images are digitized and stored on a host computer, which are then later processed.

1.4 Application Areas

The development of portable Liquid Crystal Polarization Cameras has facilitated the study of a number of new application areas in Polarization Vision revealing potential practical utility for Image Understanding, and, as a potentially valuable tool for the general study of science. On-going research is shown in four of these application areas. These are just a small subset of a number of compiled results in these areas, and are not meant to be completely conclusive– an entire paper can be easily devoted to each application. The results presented are meant to reveal some of the salient capabilities of Polarization Vision for real applications which is motivating further study and the potential utility of Polarization Vision as a new promising approach to Image Understanding. The fundamental physics-based principles upon which the application results are based are summarized. Color in some of the following figures are used to represent polarization information, while in other figures color is used as a segmentation label. Figures 6 thru 13 were sensed using the camera in Figure 4, digitized and then post processed. Figures 14 thru 17 were sensed using a liquid crystal polarization camera mounted on top of a HMMWV at Martin-Marietta Denver. Figures 18 thru 21 were sensed using the camera shown in Figure 5. Figures 22 thru 24 were sensed using a waterproofed version of the camera in Figure 4.

1.4.1 Polarization in Nature and Natural Object Recognition

Figures 6 and 7 respectively show an intensity image, and, a hue-saturation-intensity representation of the partial linear polarization image for a beach scene at sunrise, the sun is rising far to the left out of the field of view. The partial linear polarization image reveals a number of physical phenomena at work in nature that intensity and color vision are oblivious too. The vast majority of significant partial polarization in this scene comes from either ocean or sky. The laws of Rayleigh scattering of sunlight off of atmosphere dictate that skylight is nearly unpolarized in the vicinity of the sun becoming more and more partially polarized moving angularly away from the sun. According to Rayleigh the partial polarization from a patch of skylight at angle α from the sun is given by [10]:

$$\frac{\sin^2 \alpha}{1 + \cos^2 \alpha},$$

the orientation of partial linear polarization being tangent to the circle centered at the sun

8

and passing through the patch of sky. There is some depolarization caused by water and haze particles as discussed by Waterman [11]. In Figures 6 and 7 the skylight in this field of view has α in the range $45^0 - 55^0$ and is therefore significantly polarized. This scene shows how different cloud densities effect skylight polarization, and what happens when partially polarized skylight reflects off of water. Due to scattering of light in air the linear polarization content of skylight is oriented almost vertically in the image shown as variations in Cyan and Green color hue. The whiteness of the denser clouds shows that they are unpolarized, less dense clouds have some chromaticity because they are translucent with respect to background polarized skylight depolarizing this to some extent but also slightly altering the orientation of partial linear polarization of skylight. Some portions of ocean reflect light from clouds, other portions of ocean reflect light from sky. Unpolarized light from dense clouds reflects off of water with linear polarization component oriented horizontally (Magenta) while almost vertical orientation of linear po'_rization contained in skylight reflects off of water within the approximate orientation range $40 - 60^o$, shown in Blue-Purple color hues. The maximum partial polarization in Figure 7 is 45%.

Figures 8 and 9 respectively show an intensity image, and, a hue-saturation-intensity representation of the partial linear polarization image of another beach scene, this scene being at sunset. The sun is low in the sky just out of view slightly to the left of the image. The range of α in this view is from $10^o - 40^o$ and the qualitative effect of increasing partial polarization as a function of increasing α is clearly seen moving from left to right in Figure 9. The phase of partial polarization from ocean is oriented horizontal (hue Magenta) in the image while the phase of partial polarization from skylight is oriented nearly vertical (hues Cyan and Green) in the image. The horizontal phase of reflected polarization from ocean is consistent with nearly unpolarized skylight in the vicinity of the sun specularly reflecting off of water into the camera (first itemized principle at the end of Section 2). The maximum partial polarization in Figure 9 is just under 40%.

Quantitative measurements taken with our polarization camera of patches of "clear" sky show that in fact partial polarization does behave according to the Rayleigh partial polarization formula to within 10%– partial polarization is seen to be just a little less than predicted by the formula. The orientation of partial linear polarization has been verified to be quite accurate to within $\pm 5^o$. Predictions about polarization of skylight and clouds have so far been primarily theoretical, and Polarization Cameras are providing the first practical tool with which to empirically study measured polarization distributions in images of nature.

Figure 10 shows the intensity image of a river that runs between wooded hills under a cloudy (unpolarized) sky. Water is difficult to segment in natural scenes using intensity and color due to its resemblance to other elements of the scene from direct mirror reflection. Figure 11 shows the corresponding partial linear polarization image revealing that in this case practically all partial polarization comes from visible portions of river in the scene. Strongest partial polarization in Figure 11 is 30%. The phase of reflected polarization represented by hues of Magenta-Red depict a horizontal phase of reflected polarization physically consistent

with specular reflection of unpolarized skylight off of a horizontal surface (first itemized physical principle in section 2). Since water is a fluid and therefore oriented parallel to gravity this provides a physically-based methodology for segmenting water in a natural scene.

Figure 12 shows grassy terrain with intermixed patches of dirt, and rocks which are either strewn about or are protruding out from dirt. There is a white concrete path on the left side, and trees in the background underneath a cloudy sky. Exposed dirt, and rock, strongly polarize light upon reflection as opposed to grass which typically has little partial polarization. Figure 13 shows a segmentation of dirt and possible rock using partial polarization and phase of polarization information. Pixels with at least 5% partial polarization are either labeled Red or Bright White. (The criterion 5% represents "significant" partial polarization with a high confidence that the measured intensity variations between polarization components are not due to camera noise.) The phase of polarization for Red labeled pixels is within the range of $\pm 20^o$ with respect to horizontal, representing primarily level dirt patches. Bright White labeled pixels in Figure 13 have phase of polarization significantly deviant from horizontal (i.e., outside the range $\pm 20^o$) implying a polarizing surface that is tilted and therefore most probably rock. Because of the first itemized physical principle described at the end of Section 2, phase of polarization from specular reflection directly reveals the orientation of the projected surface normal onto the image plane (i.e., the surface normal is contained in the plane of incidence for smooth objects). Of course there could be level portions of rock within the Red labeled pixels, but rock protrusions must eventually have a significant tilt in some parts. The Bright White pixels in Figure 13 do truly reveal many areas where there is protruding rock or small freestanding rocks, including a significantly sized rock protrusion near the lower right corner of this image. This is important information for determining traversability for autonomous land vehicles.

1.4.2   Automatic Target Detection And Recognition

At the Lockheed-Martin, Denver facility a liquid crystal polarization camera has been installed atop one of the Semiautonomous Surrogate Vehicles (SSV) which is a HMMWV capable of traversing almost any kind of rugged terrain. The goal of the study is to create an empirical polarization image database of various Army vehicles in various poses for different viewer-solar illumination geometries. From the augmented polarization feature information contained in such a database, the study is examining how this aids both enhanced detection and enhanced recognition capabilities.

Figure 14 shows an intensity image of a camouflaged HMMWV partly occluded by a bush. The HMMWV is barely detectable in this image even to human vision. While the color and texture appearance of the Army surplus camouflage net concealing the HMMWV resembles that of the bush and background terrain, the actual material from which this net is constructed can be distinguished by its high degree of polarization reflectivity as shown

in Figure 15 with color label Magenta (i.e., segmentation obtained by thresholding above 30% partial polarization). This is one demonstration of enhanced target detection capability using polarization vision.

Figures 16 and 17 both show a HMMWV vehicle viewed about 45 degrees from a frontal view against a background of prairie grass (sun is oriented directly in front of the vehicle at about a 45 degree incident slant). Figure 16 is an intensity image, and Figure 17 is a polarization image of the same scene. Figure 17 shows a variety of polarization signatures occurring for the HMMWV, directly related to both material composition of parts of the vehicle, and orientation of these parts of the vehicle. The anti-ballistic glass on the HMMWV (as well as on other military vehicles) has particularly salient polarization properties with respect to light passing through the glass, and, light specularly reflecting off the glass. The portions of anti-ballistic glass at the left of the vehicle in Figure 17 shows initially unpolarized light from the prairie grass being polarized as it passes through the glass. Because the anti-ballistic glass is non-uniformly birefringent across the glass, different orientations of partial linear polarization produce a rainbow color pattern of lines using color visualization. Specular reflection from the anti-ballistic glass windows on the right of the HMMWV produce significant partial polarization, phase of this polarization (seen in blue) related to the orientation of the glass. Cyan and green color hues at the front of the HMMWV vehicle are primarily from rubber and other dielectric material comprising the tires, front fender, and, the radiator grill. In Figure 17 painted surfaces with surface normal oriented significantly away from the midway direction between the viewing and solar illumination directions have relatively insignificant partial polarization. Note that the painted frames around the front windshields of the HMMWV with surface normal oriented not too far from midway between the viewing and solar illumination directions, have significant partial polarization. Another salient polarization signature comes from the parabolic reflectors of the headlights producing a circular rainbow in color visualization which is visible even with few pixels making up the headlights. (The color near the back right wheel in Figure 17 is due to grass swaying in the wind and is not a real polarization effect.)

1.4.3   Automated Assessment of Damage to Ship Hulls

A very important task for the U.S. Coast Guard is the rapid assessment of damage to a ship that has run aground (e.g., the Exxon Valdez) to evaluate how to minimize further damage to the ship and to the surrounding environment. Another important task is the thorough inspection of the hulls of ships in dock for routine maintenance, identifying damage such as from scrapes and corrosion requiring repair. Currently the U.S. Coast Guard uses frogmen divers to inspect portions of ship hulls underwater, a task that can be very dangerous as well as having limited inspection access. Under consideration is the development of an underwater Remote Operated Vehicle (ROV) using sensors to automatically gather data from the ship's hull to assess damage. Under sponsorship of the U.S. Coast Guard, one of the sensors

11

currently being evaluated for use on such an ROV is a Liquid Crystal Polarization Camera because of its enhanced ability to detect exposed metal, and rust.

Figures 18 thru 21 show applications to Ship Hull Damage Assessment using the Polarization Camera in Figure 5. The intensity images in Figures 18 and 20 are of a steel panel that has been painted with a white coat of diffuse paint, and then an orange coat of diffuse paint. This application of Polarization Vision exploits how materials *depolarize* incident linear polarized light upon reflection. A polarization model predicting reflected polarization from materials as a function of any incident polarization state of light is presented in [14]. The ROV would provide its own illumination, in this case with a linear polarizer mounted on a light source. In Figures 18 thru 21 the surface normal of the steel panel in each case is parallel to the optic axis of the camera, and the illuminator is oriented parallel to viewing. Incident linear polarized light is oriented parallel in the images, this orientation really not mattering due to normal incidence of light.

In Figure 18 scrape damage has occurred on the panel, some scrapes only exposing the first layer of white paint, other scrapes penetrating all the way down to the steel metal. From the intensity image in Figure 18 it is difficult to tell which scrapes reveal only white paint and where bare metal is exposed. Reflected intensity and color look the same from these two types of damage. Diffuse reflection from paint will significantly depolarize incident linear polarized light, while linear polarization reflected from exposed metal will remain almost completely linearly polarized, especially at normal incidence. Reflected polarization from metal has partial polarization of nearly 1.0, while partial polarization from bright white paint is below 0.1. Diffuse reflection from orange paint has a partial polarization of about 0.3 . Hence, using partial polarization, scrape damage can be robustly distinguished. In Figure 19 Magenta superimposed label depicts scrape damage down to white paint layer, Green superimposed label depicts scrape damage down to steel metal. It is very important to identify where metal has been exposed from damage because of rust and corrosion that will soon occur. Color analysis cannot distinguish white paint from exposed metal under most conditions since they reflect the same color of light from the illuminator.

Figure 20 shows another part of the panel where scrape damage has occurred some of this exposing steel metal which has subsequently rusted. A good portion of this rust has leaked out over undamaged portions of the panel, but this is hard to automatically tell from intensity or color. Note that the intensity of rust at the top of Figure 20 is the same intensity as that of scrapes downto the white painted layer so that intensity properties are not enough to distinguish phenomena in this image. Also rust has the same color as the standard orange painted surface of the steel panel. Rust as it turns out has a significantly higher specular albedo than most diffuse paints, and as a result does not depolarize linearly polarized light nearly as much. In Figure 20 rusted portions of the panel have partial polarization 0.7-0.8 which readily distinguishes it from undamaged portions and scrape damage down to the first paint layer. In Figure 21 Yellow superimposed label depicts rust and Magenta superimposed label depicts scrape damage down to white paint layer. Rusted metal can

also be distinguished from recently exposed bare (i.e., unrusted) metal as rust does slightly depolarize incident linearly polarized light.

1.4.4 Marine Biology

It has been discovered over the past two decades that a number of underwater marine animals, including fish and shrimp, have significant Polarization Vision [15], [12], [16], yet the behavioral significance of this visual sensory modality remains a mystery. The Liquid Crystal Polarization Camera is providing the first comprehensive look of what the underwater world looks like in the domain of Polarization Vision, giving important insight into how many underwater animals may "see." Marine Biologists at University of Maryland- Baltimore County are studying underwater polarization vision using Polarization Camera Technology developed under ARPA funding.

Upon Snell refraction into ocean water sunlight becomes slightly polarized, but just as with polarization of skylight most polarization of light in ocean water arises from scattering [11]. In the case of ocean water the scatterers are suspended particles ranging from minerals to microscopic organisms resulting in partial linear polarization which is oriented primarily horizontal with respect to the ocean surface and having partial polarization up to as much as $50 - 60\%$ depending upon the density and types of suspended scatterers. Most marine animals underwater appear to reflect unpolarized light. To a biological or artificial sensor having Polarization Vision this can provide an advantage with respect to enhanced contrast of the unpolarized object against the significantly polarized background of seawater. Intensity and color vision become blurred the further objects are away from the viewer.

Figure 22 shows an example of a color image of fish underwater, their outlines hard to discern due to the fact that they reflect back the same color of seawater, and that the seawater is a bit "murky" from suspended particles. Figure 23 shows a partial linear polarization image of the same scene. The reddish color hue of seawater showing nearly horizontally oriented partial linear polarization while the fish themselves are almost completely achromatic. This illustrates how polarization vision may be used for contrast enhancement in biological vision systems, which may be exploited for enhanced underwater automatic target detection and recognition in certain cases. Note how the two small fish in Figure 22 (one near the top, and another to the right in the image) are almost completely invisible, while in the polarization in Figure 23 they are more apparent. The other fish have enhanced contrast as well. Apart from Image Understanding applications, a polarization camera can enhance human vision underwater.

Polarization cameras are revealing that some portions of certain marine animals reflect polarized light, which may be important to explaining some behavioral characteristics of these animals. Figure 24 shows a hue-saturation-intensity representation of a partial linear polarization image of a Mantis Shrimp (lying upside-down). Of interest are the polarizing

13

properties of the frontal antennal scales at the right of this image– in the partial linear polarization image one scale appears in color hue purple, the other scale appears in color hue yellow indicating almost a 90° difference in orientation of polarization between the two scales. Before such polarization images taken with a Polarization Camera this potentially important characteristic was not known. The origin of polarization is not from specular or diffuse reflection–it turns out that these antennal scales consist of organic micropolarizers that are built into the structure of the animal itself! The Mantis Shrimp which possesses polarization vision can vary this polarization orientation difference by moving its frontal scales and one conjecture is that this can possibly be used as a method of communication or identification. Other significant polarization effects are being noticed with starfish, and lionfish which may also have similar polarizing microstructures. Polarization cameras may reveal a potentially whole new area in Marine Biology.

1.5   Conclusions and Future Directions For Polarization Vision

Polarization Vision is a new sensory modality for image understanding that can significantly augment the capabilities of computer vision systems, as well as expand the horizons of human visual awareness. This is becoming more evident as Polarization Camera Technology matures and becomes readily available to a diverse group of researchers for use outdoors and underwater. A broad overview of recent results was presented over a diverse set of applications where either basic low-level processing, or, a natural visualization of polarization data revealed important scene information that was not as evident from intensity or color.

It is felt that Polarization Vision has not yet nearly reached its full role in Computer Vision. The full application potential of Polarization Vision will be revealed as there is wider use of Polarization Cameras in various research science areas. While Liquid Crystal Polarization Cameras are proving to be quite a practical tool for studying Polarization Vision on their own, developments are already underway for the next generation of polarization cameras utilizing more self-contained technology that will eventually produce very high-resolution polarization images at up to 1000 images a second.

2   Other Research Efforts

2.1   Diffuse Reflection Model

One of the most common assumptions for recovering object features in computer vision and rendering objects in computer graphics is that diffuse reflection from materials is Lambertian. A limitation of this work is that there is no account for the behavior of diffuse reflection in the limit as rough surfaces become mildly rough or smooth- an important and large class

14

of surfaces in practice. This paper shows that there is significant deviation from Lambertian behavior in diffuse reflection from *smooth* surfaces not predicted by existing reflectance models, having an important bearing on any computer vision technique that may utilize reflectance models including shape-from-shading and binocular stereo. In particular, contrary to prediction by Lambert's Law, diffuse reflection from smooth surfaces is significantly viewpoint dependent, and there are prominent diffuse reflection maxima effects occurring on objects when incident point source illumination is greater than 50° relative to viewing including the range from 90° to 180° where the light source is behind the object with respect to viewing. We present here a diffuse reflectance model, derived from first physical principles, that accurately predicts diffuse reflection from smooth inhomogeneous dielectric surfaces as a function of both viewing angle, and, angle of incidence. Utilizing results of radiative transfer theory for subsurface multiple scattering this new model precisely accounts for how incident light and the distribution of subsurface scattered light is influenced by Fresnel attenuation and Snell refraction at a smooth air-dielectric surface boundary. A number of experimental results have verified the proposed diffuse reflectance model.

A prevalent class of materials encountered both in common experience and in computer vision/robotics environments are inhomogeneous dielectrics which include plastics, ceramics, and, rubber. In computer vision a widely used assumption about diffuse reflection from materials is Lambert's law [17], namely the expression:

$$\frac{1}{\pi} L\rho \cos \psi d\omega$$

where ρ is termed the *diffuse albedo* in the range $[0, 1.0]$. This reflectance model is typically instantiated into the implementation of a large number of algorithms such as shape-from-shading [18] and photometric-based binocular stereo [19], [20]. It is therefore important for researchers in the computer vision community who utilize assumptions about diffuse reflection to be aware of the conditions under which there is significant deviation from Lambert's law.

Almost all diffuse reflection from inhomogeneous dielectrics physically arises from subsurface multiple scattering of light caused by subsurface inhomogeneities in index of refraction. In this paper we model inhomogeneous dielectric material as a collection of scatterers contained in a uniform dielectric medium with index of refraction different from that of air. We derive an expression for diffuse reflected radiance resulting from the process of incident light refracting into the dielectric medium across a smooth surface boundary, producing a subsurface diffuse intensity distribution from multiple internal scattering, and then refraction of this subsurface diffuse intensity distribution back out into air. We also account for the infinite progression of internal specular reflection at the air-dielectric boundary and sub-surface scattering. A common property of diffuse reflection from smooth inhomogeneous dielectric surfaces is that such reflection is azimuth independent with respect to viewing about the surface normal, regardless of the fixed direction of incident light. We have formally derived

15

and empirically verified that for smooth inhomogeneous dielectric surfaces that exhibit such azimuth symmetric diffuse reflection, if light is incident with radiance, L, at incidence angle, ψ, through a small solid angle, $d\omega$, then

$$\varrho L \times (1 - F(\psi, n)) \times \cos\psi \times (1 - F(\sin^{-1}(\frac{\sin\phi}{n}), 1/n))\, d\omega \qquad (4)$$

describes the reflected radiance into viewing angle, ϕ, (i.e., angle between viewing and the surface normal, also known as *emittance angle*) [21], [22]. The terms $F(,)$ refer to the Fresnel reflection coefficients [23], n, is the index of refraction of the dielectric medium, and, ϱ, is the *total diffuse albedo*. We showed that the total diffuse albedo, ϱ, is directly related to both the *single scattering albedo* describing the proportion of energy reradiated upon each subsurface single scattering, and, the index of refraction n. This current paper also presents a much more comprehensive set of various results demonstrating non-Lambertian diffuse reflection effects from smooth surfaces explained by expression 4.

Particularly useful to object feature extraction in computer vision, our expression 4 for diffuse reflection allows precise characterization of the conditions under which the Lambertian model breaks down for inhomogeneous dielectrics and where our more accurate model should be used. We show that Lambert's law is valid for smooth dielectrics to within 5% only as long as both angle of incidence, ψ, and viewing angle, ϕ, are simultaneously less than 50°. This means that for applications in computer vision there are a large number of situations in which Lambert's law is significantly in error– near the occluding contour of objects under any illumination condition; for illuminations incident at greater than 50° relative to viewing there will be significant errors both near the occluding contour and over a large portion of object area bounded on one side by the shadow boundary with respect to illumination; for multiple images of a smooth dielectric object there will be significant viewpoint dependence of diffuse reflection for most object-viewpoint situations. Existing diffuse reflectance models do not account for these errors. In addition to experimentally verifying the viewpoint dependence of diffuse reflection, we show how the diffuse reflection maximum occurring between an occluding contour and the shadow boundary for a smooth dielectric illuminated by a point light source is accurately predicted because of this viewpoint dependence. For illumination incident at 90° and greater relative to viewing, a diffuse reflection maximum is not even predicted by existing models having dependence only on angle of incidence, when in fact this maximum is very prominent. Furthermore, diffuse reflection is empirically observed to be very small in the immediate vicinity of an occluding contour for *all* illumination conditions, an observation that is not supported by existing models, and yet accounted for by expression 4.

2.2   Relative Strength of Diffuse and Specular Reflection

An important feature of our diffuse reflectance model is that it predicts the surface diffuse albedo for dielectrics purely in terms of physical parameters. Inhomogeneous dielectric sur-

faces exhibit both diffuse and specular reflection components. Previously, combined diffuse and specular reflection has been modeled as a sum of scaled diffuse and specular terms, with the scaling factors (i.e., *diffuse albedo* and *specular albedo*) determined from experimental fitting for each particular surface. We propose the following combined reflectance model for diffuse and specular reflected radiance from smooth surfaces [24]:

$$L \varrho \left[1 - F(\psi, n) \right] \cos \psi \left[1 - F(\sin^{-1}(\frac{\sin \phi}{n}), 1/n) \right] d\omega$$

$$+ \ L F(\psi, n) \, \delta(\psi - \phi) \, \delta(\theta_0 + 180 - \theta), \tag{5}$$

for small incident solid angle, $d\omega$, at incidence angle ψ, incident azimuth angle θ_0, emittance angle ϕ and emitted azimuth angle θ.

The combined diffuse and specular reflectance model, expression 17 can be used to formally answer the question: How bright is a specularity ? Taking the ratio of the strengths of the specular to diffuse reflection components of expression 5:

$$\frac{F(\psi, n)}{\varrho \left[1 - F(\psi, n) \right] \cos \psi \left[1 - F(\sin^{-1}(\frac{\sin \phi}{n}), 1/n) \right] d\omega} \,, \tag{6}$$

which is independent of uniform incident radiance, L. Since $F(x, n)$ and $F(x, 1/n)$ are monotonically increasing with respect to increasing x it should be clear that diffuse reflection is at a maximum when $\psi = 0^o$, $\phi = 0^o$ and specular reflection is at a minimum when $\psi = 0^o$. Therefore, the ratio expression 6 is a minimum when viewing-illumination geometry is at normal incidence and viewing. The following ratio constitutes a physical lower bound on the ratio of specular to diffuse reflected radiance:

$$\frac{F(0^o, n)}{\varrho \left[1 - F(0^o, n) \right] \left[1 - F(0^o, 1/n) \right] d\omega} \,. \tag{7}$$

The total diffuse albedo, ϱ, is largest for conservative scattering when the single scattering albedo $\rho = 1.0$. Using expression 16 to compute ϱ at $\rho = 1.0$, the physical lower bound expressed by 7 for the ratio of specular to diffuse reflected radiance evaluated for different indices of refraction is ($d\omega$ in steradians):

$$(n = 1.4) \ \frac{0.0838}{d\omega} \quad (n = 1.7) \ \frac{0.211}{d\omega} \quad (n = 2.0) \ \frac{0.370}{d\omega} \,.$$

These expressions represent physical lower bounds below which it is not physically possible to have brightness contrast between a specularity and surrounding diffuse reflection on a smooth dielectric surface. Since practically all dielectrics have $n \geq 1.4$, this particular lower bound can serve as a very conservative general formula for ruling out specularities in a scene.

2.3 3-D Stereo

We have developed a novel robust methodology for corresponding a dense set of points on an object surface from photometric values, for 3-D stereo computation of depth [25]. The methodology utilizes multiple stereo pairs of images, each stereo pair taken of exactly the same scene but under different illumination. With just 2 stereo pairs of images taken respectively for 2 different illumination conditions, a stereo pair of ratio images can be produced; one for the ratio of left images, and one for the ratio of right images. We demonstrate how the photometric ratios composing these images can be used for accurate correspondence of object points. Object points having the same photometric ratio with respect to 2 different illumination conditions comprise a well-defined equivalence class of physical constraints defined by local surface orientation relative to illumination conditions. We formally show that for diffuse reflection the photometric ratio is invariant to varying camera characteristics, surface albedo, and viewpoint and that therefore the same photometric ratio in both images of a stereo pair implies the same equivalence class of physical constraints. Corresponding photometric ratios along epipolar lines in a stereo pair of images under different illumination conditions is therefore a robust correspondence of equivalent physical constraints, and determination of depth from stereo can be performed without explicitly knowing what these physical constraints being corresponded actually are. While illumination planning is required our photometric-based stereo methodology does not require knowledge of illumination conditions in the actual computation of 3-D depth, and is applicable to perspective views. This technique extends stereo determination of 3-D depth to smooth featureless surfaces without the use of precisely calibrated lighting. We demonstrate experimental depth maps from a dense set of points on smooth objects of known ground truth shape, determined to within 1% depth accuracy.

To describe the problematic issues of comparing image intensities between a stereo pair of cameras we need to understand about the image formation process and the nature of reflection from objects. We describe the formation of image intensity values beginning with the familiar relation from Horn and Sjoberg [26]:

$$E \;=\; L_r(\pi/4)(D/i)^2 \cos^4 \alpha \;, \tag{8}$$

relating image irradiance, E, to reflected radiance, L_r. The lens diameter, D, image distance, i, and light angle, α, incident on the camera lens. Equation 8 assumes ideal pinhole optics. The effective diameter, D, of a lens can be controlled with an aperture iris the size of which is measured on an F-stop scale. Image irradiance is very sensitive to F-stop. While a stereo pair of cameras can use identical model lenses at exactly the same F-stop setting, the effective lens diameters can still be slightly different. The focal lengths as well can be slightly different and by the classical thin lens law this will influence the image distance, i, in turn effecting the image irradiance. Even in the ideal case where focal lengths are precisely equal, the image distance, i, can be slightly different for a stereo pair of images even though the images

"appear" equivalently in focus when in fact they are not precisely in focus. On top of all this is the dependence of image irradiance in perspective images on pixel location relative to the optical center of the image plane. The farther a pixel is radially away from the optical center, the larger is the light incident angle, α, which strongly effects image irradiance. Image irradiances arising from the same object point appear in different parts of a stereo pair of images making them difficult to compare.

Equation 8 only takes into account the optics involved in image formation. Image irradiance is converted into *pixel gray value* using electronics. In general the conversion of image irradiance, E, into pixel gray value, I, can be described by the expression

$$I = gE^{\frac{1}{\gamma}} + d, \tag{9}$$

where g is termed the *gain*, d is the *dark reference*, and, γ, controls the non-linearity of gray level contrast. It is typically easy to set $\gamma = 1.0$ producing a linear response, and easy to take a dark reference image with the lens cap on, then subtracting d out from captured images. However, we have observed that not only can the gain, g, be variable between identical model cameras but this can change over time especially for relatively small changes in temperature. Unless g is calibrated frequently, comparing pixel gray values for identical image irradiances between a stereo pair of cameras can be difficult.

A widely used assumption about diffuse reflection from materials is that they are Lambertian [17] meaning that light radiance, L, incident through solid angle, $d\omega$, at angle of incidence, ψ, produces reflected radiance:

$$L \rho \cos \psi \, d\omega$$

independent of viewing angle. The independence of diffuse reflected radiance with respect to viewing angle makes it theoretically feasible to associate radiance values with object points in a stereo pair of images. However, even for ideal Lambertian diffuse reflectance the above discussion outlines the practical difficulties in achieving an accurate correspondence of pixel gray values produced from reflected radiance in a stereo pair of cameras.

The physical reality of diffuse reflection makes it even more practically difficult to associate diffuse reflected radiance with object points across a stereo pair of images. A recently proposed diffuse reflectance model for smooth dielectric surfaces [21], [27], [22] empirically verified to be more accurate than Lambert's Law, expresses the dependence of diffuse reflected radiance on both angle of incidence, ψ, and viewer angle, ϕ, as

$$L \rho \left[1 - F(\psi, n)\right] \cos \psi \left[1 - F(\sin^{-1}(\frac{\sin \phi}{n}), 1/n)\right] d\omega \tag{10}$$

where the functions, $F()$, are the Fresnel reflection coefficients [23], and, n, is the index of refraction of the dielectric surface, and, ρ, is the diffuse albedo. Diffuse reflected radiance

from an object point as seen from the two different viewpoints of a stereo pair of cameras will almost always not be equal.

Combining equations 8, 9 and 10 gives us an expression which precisely relates pixel gray value, I, to diffuse reflection as a function of imaging geometry and camera parameters. For incident radiance L through a small solid angle, $d\omega$, at an angle of incidence, ψ, the gray value formed from viewing angle, ϕ (assuming we subtract out the dark reference, d) is:

$$I = g \left[(\pi/4)(D/i)^2 \cos^4 \alpha \, L \rho [1 - F(\psi, n)] \times \cos \psi \times [1 - F(\sin^{-1}(\frac{sin\phi}{n}), 1/n)] \, d\omega \right]^{1/\gamma}$$

For a general incident radiance distribution, $L(\psi, \theta)$, (θ is azimuth about the surface normal) with respect to an object point, integrating over the incident hemisphere, the gray value will be:

$$I = g \left[(\pi/4)(D/i)^2 \cos^4 \alpha \int L(\psi, \theta) \, \rho [1 - F(\psi, n)] \times \cos \psi \times [1 - F(\sin^{-1}(\frac{sin\phi}{n}), 1/n)] \, d\omega \right]^{1/\gamma}$$

$$= g \left[(\pi/4)(D/i)^2 \cos^4 \alpha \, [1 - F(\sin^{-1}(\frac{sin\phi}{n}), 1/n)] \, \rho \right]^{1/\gamma} \times \left[\int L(\psi, \theta) \, [1 - F(\psi, n)] \, \cos \psi \, d\omega \right]^{1/\gamma}$$
(11)

Consider this object point first illuminated with an incident radiance distribution, $L_1(\psi, \theta)$, and then illuminated with an incident radiance distribution, $L_2(\psi, \theta)$. From equation 11 the photometric ratio of gray values is:

$$\frac{I_1}{I_2} = \frac{\left[\int L_1(\psi, \theta) \, [1 - F(\psi, n)] \, \cos \psi \, d\omega \right]^{1/\gamma}}{\left[\int L_2(\psi, \theta) \, [1 - F(\psi, n)] \, \cos \psi \, d\omega \right]^{1/\gamma}}$$
(12)

where the terms outside the integral signs in the numerator and the denominator cancel out. This photometric ratio expresses a well-defined physical constraint determined by an illumination distribution relative to surface orientation at an object point. It is a function of only incident light geometry relative to local surface orientation, and is invariant to all camera parameters (except γ), viewing angle, ϕ, and diffuse surface albedo, ρ. Note that this photometric ratio is local to an object surface point, so that it does not matter if the incident lighting distribution changes from object point to object point (i.e., which can occur if lighting elements are close to the object relative to object size). This photometric ratio is an invariant with respect to each object point.

20

2.4   Segmenting Curvature

Gaussian curvature is an intrinsic local shape characteristic of a smooth object surface that is invariant to orientation of the object in 3-D space and viewpoint. Accurate determination of the sign of Gaussian curvature at each point on a smooth object surface (i.e., the identification of *hyperbolic, elliptical* and *parabolic* points) can provide very important information for both recognition of objects in automated vision tasks and manipulation of objects by a robot. We present a multiple illumination technique that directly identifies elliptical, hyperbolic, and parabolic points from diffuse reflection from a smooth object surface. This technique is based upon a photometric invariant involving the behavior of the image intensity gradient under varying illumination under the assumption of the image irradiance equation. The nature of this photometric invariant allows direct segmentation of a smooth object surface according to the sign of Gaussian curvature independent of knowledge of local surface orientation, independent of diffuse surface albedo, and with only approximate knowledge of the geometry of multiple incident illumination. In comparison with photometric stereo, this new technique determines the sign of Gaussian curvature directly from image features without having to derive local surface orientation, and, does not require calibration of the reflectance map from an object of known shape of similar material or precise knowledge of all incident illuminations. We demonstrate how this segmentation technique works under conditions of simulated image noise, and actual experimental imaging results.

Horn and Sjoberg [26] defined the *image irradiance equation* which equates image ir-radiance, $I(x, y)$, to reflected radiance, $R(p, q)$ up to a multiplicative constant involving camera parameters. Assuming that this constant factor is known and incorporated into the reflectance map, then

$$I(x, y) \ = \ R(p, q) \tag{13}$$

which for a known reflectance map allows the derivation of a surface orientation constraint in terms of gradient variables, p and q from the image irradiance at a pixel. In the case of the Lambert reflectance map, expression 9, the surface orientation constraint derived from an image irradiance value is a quadratic expression in p and q. Therefore, the quantitative derivation of surface orientation from such local information is underconstrained to an infinity of possible orientations along a quadratic curve in gradient space.

As local surface orientation is related to the first order variation of the surface height function, $f(x, y)$, local surface curvature is related to the first order variation of surface orientation (which in turn involves second order variations in the height function). Constraints on surface curvature can be obtained photometrically by equating the derivatives of the image irradiance equation 13. Making the following notational simplifications

$$I_x \equiv \partial I/\partial x, \quad I_y \equiv \partial I/\partial y, \quad R_p \equiv \partial R/\partial p, \quad R_q \equiv \partial R/\partial q,$$

21

the following matrix equation is obtained from the chain rule:

$$\begin{pmatrix} I_x \\ I_y \end{pmatrix} = \begin{pmatrix} \partial p/\partial x & \partial q/\partial x \\ \partial p/\partial y & \partial q/\partial y \end{pmatrix} \begin{pmatrix} R_p \\ R_q \end{pmatrix} . \tag{14}$$

The matrix in equation 14 is the *viewer centered curvature matrix*, which is also the Hessian matrix with respect to the height function, $f(x, y)$. Because the second order differentiation of $f(x, y)$ by x and by y is commutative, the off-diagonal components of the viewer centered curvature matrix, $\partial p/\partial y$ and $\partial q/\partial x$, are equal. Hence, the viewer centered curvature matrix is equivalent to the Jacobian of the transformation between image coordinates (x, y) and gradient coordinates (p, q). When the viewer centered curvature matrix multiplies an infinitesimal vector in image coordinates, the resulting vector is the corresponding infinitesimal vector change in surface orientation represented in gradient coordinates:

$$\begin{pmatrix} \partial p/\partial x & \partial p/\partial y \\ \partial q/\partial x & \partial q/\partial y \end{pmatrix} \begin{pmatrix} dx \\ dy \end{pmatrix} = \begin{pmatrix} dp \\ dq \end{pmatrix}$$

The viewer centered curvature matrix therefore relates a change in image coordinates to the corresponding change in local surface orientation at a smooth surface point. From a single image the three independent components of the viewer centered curvature matrix can be constrained by two linear equations, produced from the matrix equation 14, from measurement of the image intensity gradient.

An *object centered* curvature matrix can be defined as the matrix which multiplies an infinitesimal vector in the tangent plane at a smooth object point to produce the corresponding vector change in the surface normal. The determinant of this object centered curvature matrix is the Gaussian curvature at a point on a smooth object surface which can be shown to be a fundamental invariant of the surface with respect to how it is oriented in 3-D space [28]. When expressed in terms of gradient variables relative to a set of image coordinates, the Gaussian curvature at a point is given by:

$$\frac{(\partial p/\partial x)(\partial q/\partial y) - (\partial p/\partial y)(\partial q/\partial x)}{(1 + p^2 + q^2)^2} . \tag{15}$$

It is very important to note that the sign of the Gaussian curvature is the same as the sign of the determinant of the viewer centered curvature matrix in equation 14.

We consider the extension of matrix equation 14 incorporating two reflectance maps, $R^1(p, q)$, and $R^2(p, q)$:

$$\begin{pmatrix} I_x^1 & I_x^2 \\ I_y^1 & I_y^2 \end{pmatrix} = \begin{pmatrix} \partial p/\partial x & \partial q/\partial x \\ \partial p/\partial y & \partial q/\partial y \end{pmatrix} \begin{pmatrix} R_p^1 & R_p^2 \\ R_q^1 & R_q^2 \end{pmatrix} . \tag{16}$$

Each of the two image intensity gradients is produced at an object point respective to each of the reflectance maps. Labeling the matrices in equation 16 respectively from left to right as A, B, and, C so that

$$A = BC,$$

we will refer to matrix A as the *image intensity gradient matrix*, and to matrix C as the *reflectance map gradient matrix*. It is clear that

$$\text{DETERMINANT}(A) = \text{DETERMINANT}(B) \times \text{DETERMINANT}(C).$$

Therefore, if the determinant of the reflectance map gradient matrix is known for a given surface orientation, then the sign of the determinant of the viewer centered curvature matrix (and therefore the sign of the Gaussian curvature) can be derived from the computation of the determinant of the image intensity gradient matrix. Suppose that two reflectance maps $R^1(p,q)$ and $R^2(p,q)$ are produced from two different incident illuminations. If the determinant of the reflectance map gradient matrix has the same known sign for all surface orientations p, q, then the sign of Gaussian curvature can be determined from the determinant of the measured intensity image gradient matrix independent of local surface orientation. So, for example, if the determinant of the reflectance map gradient matrix were consistently positive for all surface orientations, a positive, negative, zero determinant for the measured image intensity gradient matrix respectively identifies a(n) elliptical, hyperbolic, parabolic point.

The determination of the sign of Gaussian curvature from equation 16 has a direct geometric interpretation in terms of the rotational change of the image intensity gradient induced by varying illumination. The value of the determinant of the image intensity gradient matrix is equal to the z-component of the cross-product of the two image intensity gradients as vectors in the x-y image plane. That is:

$$DETERMINANT \begin{pmatrix} I_x^1 & I_x^2 \\ I_y^1 & I_y^2 \end{pmatrix} = I_x^1 I_y^2 - I_y^1 I_x^2$$

$$(I_x^1, I_y^1, 0) \times (I_x^2, I_y^2, 0) = (0, 0, I_x^1 I_y^2 - I_y^1 I_x^2),$$

where '$\times$' is the vector cross-product operation. Therefore

$$I_x^1 I_y^2 - I_y^1 I_x^2 = \|(I_x^1, I_y^1, 0)\| \cdot \|(I_x^2, I_y^2, 0)\| \sin \theta,$$

where θ is the angle between the image intensity gradient vectors. Hence, the sign of the determinant of the image intensity gradient matrix is equal to the sign, θ, of the rotational

change between the image intensity gradient vectors before and after the change in illumination. For a fixed sign of the determinant of the reflectance map gradient matrix in equation 16, the direction of rotational change of the image intensity gradient at an object point is determined by the sign of the Gaussian curvature at that point. At parabolic points the determinant of the viewer centered curvature matrix is zero and therefore there is no rotational change.

As discussed in the previous section, the Lambert reflectance map (expression 9) provides a good approximation to the relationship between surface orientation and diffuse reflection from smooth and mildly rough dielectric surfaces for incident point source illumination directions not too oblique with respect to viewing. Unfortunately the sign of the determinant of the reflectance map gradient matrix in equation 16 for Lambertian reflectance using any pair of different incident point source orientations is not the same with respect to *all* surface orientations. An easy proof of this is to see that the determinant of the reflectance map gradient matrix for Lambertian reflectance is zero for surface orientations p, q equal to any of the two incident point source orientations that are used. If it is known *a priori* what restricted range of surface orientations will be examined it may be possible to use two incident point source orientations that will produce a Lambertian reflectance gradient matrix having determinant the same sign over this range of surface orientations. Our goal however is to come up with a general technique for finding the sign of Gaussian curvature completely invariant to all surface orientations.

A sub-class of reflectance maps that results in a reflectance map gradient matrix whose sign of determinant is invariant to all surface orientations is part of what we term the class of *Ratio-Of-Lambertian* reflectance maps. Consider the ratio of Lambertian reflectance maps, expression 9, for two incident point source orientations p_s, q_s, and, p'_s, q'_s resulting in:

$$R(p,q) \; = \; \frac{L_i}{L'_i} \frac{1 + pp_s + qq_s}{1 + pp'_s + qq'_s} \frac{\sqrt{1 + p_s^2 + q_s^2}}{\sqrt{1 + (p'_s)^2 + (q'_s)^2}} \, . \tag{17}$$

The Ratio-Of-Lambertian reflectance map does not physically exist for a single image of a diffuse reflecting surface, but rather for the ratio of two images of a Lambertian diffuse reflecting surface each image taken under a different incident point source illumination. Note that this reflectance map is invariant to albedo, ρ. It is also invariant to perspective effects of the radiometry of image formation, (i.e.,the $\cos^4 \alpha$ effect discussed by Horn and Sjoberg [26] gets factored out for each pixel). In the case where $p'_s = q'_s = 0$, that is one of the incident illumination directions is parallel to viewing, the Ratio-Of-Lambertian reflectance map becomes

$$R(p,q) \; = \; \frac{L_i}{L'_i}(1 + pp_s + qq_s)\sqrt{1 + p_s^2 + q_s^2} \tag{18}$$

which is completely linear in gradient variables p and q. As a height function above the $p-q$

24

plane the sub-class of reflectance maps represented by expression 18 are ramp functions with the gradient, (R_p, R_q), of the ramp equal to a constant scalar multiple of the vector (p_s, q_s).

From expression 10, in actuality the Ratio-Of-Lambertian reflectance map of expression 18 is multiplied by the ratio

$$\frac{1 - F(\psi, n)}{1 - F(\psi', n)},\tag{19}$$

where ψ' is the angle of incidence with respect to the illumination parallel to viewing, and ψ is the angle of incidence with respect to the other light source. Notice that the viewing dependence, ϕ, completely cancels out. It turns out that the ratio in expression 19 is nearly constant at 1.0 for all surface orientations within the wide range of 75° relative to viewing.

Consider taking images of a diffuse reflecting object with respect to incident point source orientations, (p_1, q_1), and, (p_2, q_2). Each of these images are then divided by a third image taken for incident illumination parallel to viewing. Utilizing the Ratio-Of-Lambertian reflectance map, expression 18, the reflectance map gradient matrix is

$$C \quad = \quad \begin{pmatrix} \frac{L_1}{L_3} p_1 \sqrt{1 + p_1^2 + q_1^2} & \frac{L_2}{L_3} p_2 \sqrt{1 + p_2^2 + q_2^2} \\ \frac{L_1}{L_3} q_1 \sqrt{1 + p_1^2 + q_1^2} & \frac{L_2}{L_3} q_2 \sqrt{1 + p_2^2 + q_2^2} \end{pmatrix},\tag{20}$$

where L_1, L_2, and, L_3 are the incident radiances of the first, second, and, third point light sources respectively. Not only is this matrix constant and therefore the sign of its determinant independent of surface orientation, but there is a nice intuitive relationship between the rotational change in orientation of incident point light source illumination and the induced rotational change in image intensity gradient with respect to the ratio images:

$$DET(C) \quad = \quad \frac{L_1 L_2}{(L_3)^2} \sqrt{1 + p_1^2 + q_1^2} \sqrt{1 + p_2^2 + q_2^2} \ DET(\begin{pmatrix} p_1 & p_2 \\ q_1 & q_2 \end{pmatrix}).$$

A positive rotational component difference between (p_1, q_1) and (p_2, q_2) makes the reflectance gradient matrix have positive determinant, inducing a positive rotation in the image intensity gradient in the ratio image at elliptical points, a negative rotation at hyperbolic points, and no rotation at parabolic points. In general, for a non-zero rotational component between incident point source orientations (p_1, q_1) and (p_2, q_2), the image intensity gradient in the ratio images will always have a non-zero rotational change in the same direction as that for the point sources at elliptical points, a non-zero rotational change retrograde to that for the point sources at hyperbolic points, and no rotational change at parabolic points. The exact values for (p_1, q_1) and (p_2, q_2) need never be known, only their relative rotational orientation about the viewing direction. The only computation required are the orientations of image intensity gradients in the ratio images, which are albedo invariant.

If the third light source incident orientation is not parallel to viewing then the sign of the determinant of the reflectance map gradient matrix using the Ratio-Of-Lambertian reflectance map will not be invariant for all surface orientations. There is however good invariance of the sign of the determinant over a wide range of surface orientations if the third light source is approximately parallel to viewing- a slight deviation from the viewing direction only effects a very small range of points at occluding contours with no effect at all on other points. The restriction of having the third light source parallel to viewing is not at all bad considering that the sign of Gaussian curvature only has a chance to be determined for surface orientations that are mutually illuminated by all three light sources. It is therefore preferable to have one of the light sources parallel to viewing since it maximally illuminates all possible surface orientations that are visible.

References

[1] K. Koshikawa and Y. Shirai. A model-based recognition of glossy objects using their polarimetric properties. *Advances in Robotics*, 2(2), 1987.

[2] W. Egan. *Polarization Measurement for Remote Sensing*. McGraw-Hill, 1985.

[3] B.F. Jones and P.T. Fairney. Recognition of shiny dielectric objects by analyzing the polarization of reflected light. *Image and Vision Computing Journal*, 7(4):253–258, 1989.

[4] L.B. Wolff. *Polarization Methods in Computer Vision*. PhD thesis, Columbia University, January 1991.

[5] L.B. Wolff and T.A. Mancini. Liquid crystal polarization camera. In *Proceedings of the IEEE Workshop on Applications of Computer Vision*, pages 120–127, Palm Springs, California, December 1992.

[6] L.B. Wolff. Polarization camera technology. In *Proceedings of the DARPA Image Understanding Workshop*, pages 1031–1036, Washington, D.C., April 1993.

[7] L.B. Wolff. Polarization camera for computer vision using a beam-splitter. *Journal of the Optical Society of America, (JOSA) A, Special Issue on Physics Based Machine Vision*, 11(11):2935–2945, November 1994.

[8] G. D. Bernard and R. Wehner. Functional similarities between polarization vision and color vision. *Vision Res.*, 17:1019–1028, 1977.

[9] L.B. Wolff and A. Andreou. Polarization camera sensors. *Image and Vision Computing Journal*, August 1995.

[10] M. Born and E. Wolf. *Principles of Optics*. Pergamon Press, 1959.

[11] T.H. Waterman. Polarization sensitivity. *Handbook of Sensory Physiology, Volume 7 Part 6b Vision of Invertebrates, Edited by H.J. Altrum, Springer Verlag*, pages 283–463, 1981.

[12] J. Marshall and T. Cronin. The compound eyes of mantis shrimp i: Compound eye structure: The detection of polarized light. *Trans. of Royal Soc. B*, 334:33–56, 1991.

[13] L.B. Wolff and T.E. Boult. Constraining object features using a polarization reflectance model. *IEEE Transactions on Pattern Analysis and Machine Intelligence (PAMI)*, 13(7):635–657, July 1991.

[14] L.B. Wolff. Surface orientation from polarization images. In *Proceedings of Optics, Illumination and Image Sensing for Machine Vision II, Volume 850*, pages 110–121, Cambridge, Massachusetts, November 1987. SPIE.

[15] D.A. Cameron and E.N. Pugh. Double cones as a basis for a new type of polarization vision in vertebrates. *Nature*, 353:161–164, September 1991.

[16] C.W. Hawryshyn. Polarization vision in fish. *American Scientist*, 80:164–175, March-April 1992.

[17] J. H. Lambert. Photometria sive de mensura de gratibus luminis, colorum et umbrae. *Augsberg, Germany: Eberhard Klett*, 1760.

[18] B.K.P. Horn and M.J. Brooks. *Shape From Shading*. MIT Press, 1989.

[19] W.E.L. Grimson. Binocular shading and visual surface reconstruction. *Computer Vision Graphics and Image Processing*, 28(1):19–43, 1984.

[20] G.B. Smith. Stereo integral equation. In *Proceedings of the AAAI*, pages 689–694, 1986.

[21] L.B. Wolff. Diffuse reflection. In *Proceedings of IEEE Conference on Computer Vision and Pattern Recognition (CVPR)*, pages 472–478, Urbana-Champaign Illinois, June 1992.

[22] L.B. Wolff. A diffuse reflectance model for smooth dielectrics. *Journal of the Optical Society of America, (JOSA) A, Special Issue on Physics Based Machine Vision*, 11(11):2956–2968, November 1994.

[23] R. Siegal and J.R. Howell. *Thermal Radiation Heat Transfer*. McGraw-Hill, 1981.

[24] L.B. Wolff. Relative brightness of specular and diffuse reflection. *Optical Engineering*, 33(1):285–293, January 1994.

[25] L.B. Wolff and E. Angelopoulou. Three-dimensional stereo by photometric ratios. *Journal of the Optical Society of America, (JOSA) A, Special Issue on Physics Based Machine Vision*, 11(11):3069–3078, November 1994.

[26] B.K.P. Horn and R.W. Sjoberg. Calculating the reflectance map. *Applied Optics*, 18(11):1770–1779, June 1979.

[27] L.B. Wolff. Diffuse and specular reflection. *Proceedings of the DARPA Image Understanding Workshop*, pages 1025–1030, April 1993.

[28] M.P. do Carmo. *Differential Geometry of Curves and Surfaces*. Prentice Hall, 1976.

DISTRIBUTION LIST

addresses	number of copies

ATTN: MR. PETER J. COSTIANES
ROME LABORATORY/IRRE
32 HANGAR ROAD
ROME NY 13441-4114

5

ATTN: DR. LAWRENCE B. WOLF
COMPUTER VISION LABORATORY
DEPARTMENT OF COMPUTER SCIENCE
THE JOHNS HOPKINS UNIVERSITY
BALTIMORE MD 21218

5

ROME LABORATORY/SUL
TECHNICAL LIBRARY
26 ELECTRONIC PKY
ROME NY 13441-4514

1

ATTENTION: DTIC-OCC
DEFENSE TECHNICAL INFO CENTER
8725 JOHN J. KINGMAN ROAD, STE 0944
FT. BELVOIR, VA 22060-6218

2

ADVANCED RESEARCH PROJECTS AGENCY
3701 NORTH FAIRFAX DRIVE
ARLINGTON VA 22203-1714

1

ATTN: RAYMOND TADROS
GIDEP
P.O. BOX 8000
CORONA CA 91718-8000

1

AFIT ACADEMIC LIBRARY/LDEE
2950 P STREET
AREA B, BLDG 642
WRIGHT-PATTERSON AFB OH 45433-7765

1

ATTN: R.L. DENISON
WRIGHT LABORATORY/MLPO, BLDG. 651
3005 P STREET, STE 6
WRIGHT-PATTERSON AFB OH 45433-7707

1

```
WRIGHT LABORATORY/MTM, BLDG 653          1
2977 P STREET, STE 6
WRIGHT-PATTERSON AFB OH 45433-7739


ATTN: GILBERT G. KUPERMAN               1
AL/CFHI, BLDG. 248
2255 H STREET
WRIGHT-PATTERSON AFB OH 45433-7022


US ARMY STRATEGIC DEFENSE COMMAND       1
CSSD-IM-PA
P.O. BOX 1500
HUNTSVILLE AL 35807-3801


NAVAL AIR WARFARE CENTER                1
6000 E. 21ST STREET
INDIANAPOLIS IN 46219-2189


COMMANDING OFFICER                      1
NCCOSC RDT&E DIVISION
ATTN: TECHNICAL LIBRARY,CODE 0274
53560 HULL STREET
SAN DIEGO CA 92152-5001

COMMANDER, TECHNICAL LIBRARY            1
4747000/C0223
NAVAIRWARCENWPNDIV
1 ADMINISTRATION CIRCLE
CHINA LAKE CA 93555-6001

SPACE & NAVAL WARFARE SYSTEMS           2
COMMAND (PMW 178-1)
2451 CRYSTAL DRIVE
ARLINGTON VA 22245-5200


SPACE & NAVAL WARFARE SYSTEMS           1
COMMAND, EXECUTIVE DIRECTOR (PD13A)
ATTN: MR. CARL ANDRIANI
2451 CRYSTAL DRIVE
ARLINGTON VA 22245-5200

CDR, US ARMY MISSILE COMMAND            2
RSIC, BLDG. 4484
AMSMI-RD-CS-R, DOCS
REDSTONE ARSENAL AL 35898-5241
```

ADVISORY GROUP ON ELECTRON DEVICES   1
SUITE 500
1745 JEFFERSON DAVIS HIGHWAY
ARLINGTON VA 22202

REPORT COLLECTION, CIC-14   1
MS P364
LOS ALAMOS NATIONAL LABORATORY
LOS ALAMOS NM 87545

AEDC LIBRARY   1
TECHNICAL REPORTS FILE
100 KINDEL DRIVE, SUITE C211
ARNOLD AFB TN 37389-3211

COMMANDER   1
USAISC
ASHC-IMD-L, BLDG 61801
FT HUACHUCA AZ 85613-5000

AFIWC/MSO   1
102 HALL BLVD, STE 315
SAN ANTONIO TX 78243-7016

NSA/CSS   1
K1
FT MEADE MD 20755-6000

PHILLIPS LABORATORY   1
PL/TL (LIBRARY)
5 WRIGHT STREET
HANSCOM AFB MA 01731-3004

THE MITRE CORPORATION   1
ATTN: E. LADURE
D460
202 BURLINGTON RD
BEDFORD MA 01732

DUSD(P)/DTSA/DUTD
ATTN: PATRICK G. SULLIVAN, JR.
400 ARMY NAVY DRIVE
SUITE 300
ARLINGTON VA 22202

MISSION

OF

ROME LABORATORY

Mission. The mission of Rome Laboratory is to advance the science and technologies of command, control, communications and intelligence and to transition them into systems to meet customer needs. To achieve this, Rome Lab:

   a. Conducts vigorous research, development and test programs in all applicable technologies;

   b. Transitions technology to current and future systems to improve operational capability, readiness, and supportability;

   c. Provides a full range of technical support to Air Force Materiel Command product centers and other Air Force organizations;

   d. Promotes transfer of technology to the private sector;

   e. Maintains leading edge technological expertise in the areas of surveillance, communications, command and control, intelligence, reliability science, electro-magnetic technology, photonics, signal processing, and computational science.

The thrust areas of technical competence include: Surveillance, Communications, Command and Control, Intelligence, Signal Processing, Computer Science and Technology, Electromagnetic Technology, Photonics and Reliability Sciences.